PAPER

Check for updates

In situ hydrogen production in all-level-humidity air: integrating atmospheric water harvesting with photocatalysis†

Xueli Yan,[a] Li Tian,[a] Fei Xue,[a] Jie Huang,[a] Rui Zhao,[a] Xiangjiu Guan,*[a] Jinwen Shi, [ID] *[a] Wenshuai Chen [ID] *[c] and Maochang Liu [ID] *[ab]

H₂ production from air holds great promise as a sustainable method for green energy harvesting. However, its widespread adoption faces challenges in realizing mobile, distributed, community-managed, off-grid in situ H₂ production systems. Here, we report a bilayer nanofibrillated cellulose composite gel incorporating lithium chloride hygroscopic salt and a supported $SrTiO_3$:Al photocatalyst (denoted as NLS), designed specifically for in situ photocatalytic splitting of atmospheric water to produce H₂, using only naturally occurring moisture and sunlight. The NLS gel features a self-supply of atmospheric water, spectral splitting for efficient solar energy delivery and complementary utilization, instantaneous H₂ evolution, and stable catalyst immobilization. As a result, the NLS bilayer gel successfully achieves in situ H₂ production in full-range-humidity environments, demonstrating a hygroscopicity of 4.26 g_{H_2O} $g_{sorbent}^{-1}$ and an H₂ production activity of 65.45 μmol h⁻¹ in a 90% relative humidity environment, achieving a solar-to-hydrogen efficiency of up to 0.3%. This work represents a promising step towards realizing in situ H₂ production from air across varying humidity levels, independent of geographical constraints.

Broader context

H₂ production from ambient moisture offers substantial benefits for meeting the energy needs of isolated, off-grid regions due to the prevalence of atmospheric water. Traditional technologies have relied on external energy or material inputs, without achieving clean and portable in situ H₂ production from air. Maximizing the efficiency of in situ H₂ production from air remains a significant challenge. Here, we develop a bilayer nanocellulose composite gel, designated NFC@LiCl-SrTiO₃:Al or NLS, for photocatalytic splitting of atmospheric water to produce hydrogen, utilizing only in situ moisture and sunlight. The NLS demonstrates a solar-to-hydrogen conversion efficiency of up to 0.3% by integrating atmospheric water self-supply, optimized light delivery, and stable catalyst immobilization. This advancement represents a significant step forward for mobile, distributed, community-managed H₂ production from air in off-grid settings.

1. Introduction

The development of green energy harvesting technologies with low carbon emissions has garnered significant attention as a means to alleviate global energy scarcity and environmental pollution.[1] H₂, characterized by high energy density, cleanliness,

[a] International Research Center for Renewable Energy & State Key Laboratory of Multiphase Flow in Power Engineering, Xi'an Jiaotong University, Xi'an 710049, P. R. China. E-mail: xj-guan@mail.xjtu.edu.cn, jinwen_shi@mail.xjtu.edu.cn

[b] Suzhou Academy of Xi'an Jiaotong University, Suzhou 215123, P. R. China.
E-mail: maochangliu@mail.xjtu.edu.cn

[c] Key Laboratory of Bio-based Material Science and Technology, Ministry of Education, Northeast Forestry University, Harbin 150040, P. R. China.
E-mail: chenwenshuai@nefu.edu.cn

† Electronic supplementary information (ESI) available. See DOI: https://doi.org/10.1039/d4ey00258j

and ease of storage and transportation, is internationally recognized as a superior energy carrier.[2,3] However, there is an urgent need to achieve clean and portable in situ H₂ production to ensure on-demand supply, particularly in isolated and remote regions. Solar energy represents an abundant and virtually limitless resource of clean energy. Atmospheric water, originating from oceans, lakes, and rivers, accounts for roughly 10% of the world's total freshwater resources and is readily accessible at any time and place.[4–6] The prospect of harnessing atmospheric moisture and sunlight to product H₂ from air holds great promise in addressing the energy needs of isolated off-grid areas.

Solar-driven photocatalytic splitting of atmospheric water for H₂ production is emerging as a promising alternative to energy extraction from air.[7] This technology integrates atmospheric water harvesting (AWH) and photocatalytic H₂ production, using solar energy and atmospheric water as primary inputs, respectively,

thus eliminating the demand for an intermediate energy source. However, most of the existing photocatalytic atmospheric water splitting systems require constant replenishment of sacrificial agents, limiting their application scenarios.[8,9] In addition, the reaction mechanism of the catalyst, especially at the oxidizing end, remains unclear in H_2 production from air, which is critical for advancing the technology at the molecular level.[10] Therefore, realizing mobile, distributed, community-managed, off-grid, *in situ* H_2 production from air at different humidity levels, along with identifying corresponding mechanisms, is highly desirable.

Herein, we developed a nanofibrillated cellulose (NFC) composite gel, NFC@LiCl-SrTiO$_3$:Al (referred to as NLS), using a solution displacement method combined with freeze-drying, for H_2 production from air across varying humidity levels. The NLS gel comprises an upper layer made of the SrTiO$_3$:Al photocatalyst and a supportive hygroscopic layer composed of a hydrophilic NFC network embedded with distributed lithium chloride (LiCl). The NLS achieves H_2 production from air in varying humidity environments, demonstrating a hygroscopicity of 4.26 $g_{H_2O}\ g_{sorbent}^{-1}$ in 90% relative humidity (RH) and providing a corresponding H_2 production rate of up to 65.45 μmol h^{-1}. The solar-to-hydrogen (STH) efficiency reaches 0.3%. These capabilities stem from the ability of NLS to self-supply atmospheric water, optimize light absorption, utilize solar energy complementarily across different frequencies, facilitate H_2 evolution, and maintain catalyst stability. Furthermore, the SrTiO$_3$:Al in NLS produces reactive oxygen species (ROS) at its oxidized surface, which interacts with atmospheric water molecules. Consequently, the NLS design offers a sustainable pathway for H_2 production under all-level humidity conditions, utilizing solely *in situ* resources from the natural environment.

2. Results and discussion

2.1. Material design for solar-powered *in situ* H_2 production coupling AWH

We first proposed a bilayer NLS composite gel designed for the combination of AWH and solar H_2 production from air with all humidity levels for efficient energy-mass transfer and conversion (Fig. S1, ESI†). The upper layer of the bilayer structure is crafted from the SrTiO$_3$:Al photocatalyst while the substrate layer consists of a porous hydrophilic NFC network embedded with distributed LiCl. This design enables the NLS to serve as a reliable water source for the photocatalyst by extracting water molecules from air, leveraging its inherent hygroscopic properties and the interconnected porous network of particles and polymer nanofibers (Fig. 1(i)). The incorporation of micrometer-sized hygroscopic LiCl particles throughout both the peripheral and internal regions of the gel enables rapid surface absorption of water molecules from the atmosphere.[11] As moisture absorption increases, water molecules aggregate, liquefy, and gradually dissolve the LiCl particles.
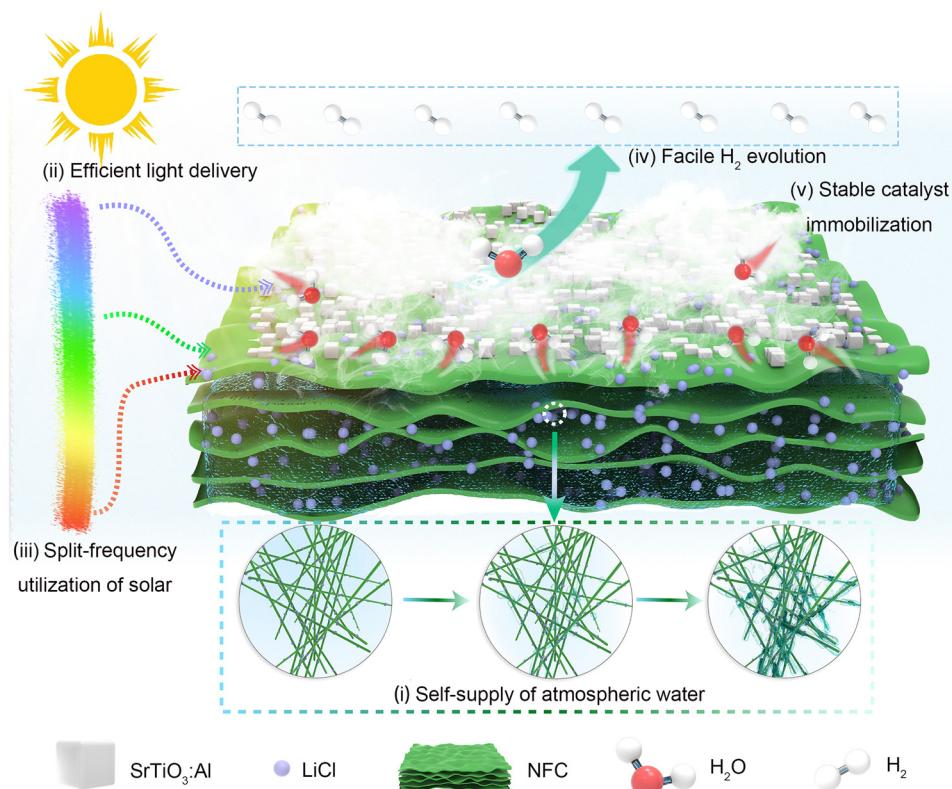

Fig. 1 Schematic illustration of the NLS gel and its application in solar-powered *in situ* H_2 production from air. (i) Self-supply of atmospheric water, *i.e.*, absorption of water vapor from the air, liquefaction, liquid water transport and storage, (ii) efficient light delivery, (iii) complementary utilization of solar energy in split frequency, (iv) facile H_2 evolution, and (v) stable catalyst immobilization.

The NFC contributes significantly to this process by virtue of its abundant surface hydroxyl groups, which exhibit strong hydrophilicity. These groups facilitate hydrogen bonding with neighboring water molecules to form bound water. Moreover, the NFC network provides structural integrity, essential for supporting the overall gel framework.[12–14] Liquid water generated through these mechanisms is efficiently transported within the NFC network by capillary forces, ensuring its distribution throughout the interior of NLS and subsequent storage within the gel structure.[15] Overall, the interconnected porous architecture constructed by nanofibers and particles plays a pivotal role in enhancing the gel's hygroscopic properties, promoting water aggregation and liquefaction, and facilitating effective water transport and storage.[13]

The water molecules harvested from air by NLS are released under sunlight irradiation. During the desorption-photocatalytic process for H_2 production, a continuous vapor of water molecules escapes from the surface of NLS upon contact with $SrTiO_3$:Al photocatalyst. From the perspective of energy flow, the NLS fully harnesses solar energy. This upper photocatalytic layer of the NLS efficiently transmits light while minimizing light attenuation caused by water and reducing thermal energy loss (Fig. 1(ii)).[16] The design of NLS realizes complementary utilization of solar energy: long-wave radiation drives AWH to achieve efficient conversion of solar energy into thermal energy, while short-wave radiation induces photocatalytic water splitting for H_2 production, enabling the effective conversion of solar energy into chemical energy (Fig. 1(iii)). Furthermore, considering the mass flow, the interface among water vapor, photocatalyst, H_2 during the NLS water desorption-H_2 production process facilitates easy diffusion of H_2 by reducing the photocatalytic reaction barrier as well as the transport resistance of both water and H_2 (Fig. 1(iv)). Clearly, the designed NLS integrates AWH and H_2 production. Particularly, the nanofabricated hygroscopic gel, NFC@LiCl (denoted as NL), can immobilize the photocatalyst effectively over extended periods to sustain its activity (Fig. 1(v)).

2.2. Synthesis and characterization of the NLS composite gel

NLS-x, where x represents the mass of $SrTiO_3$:Al in NLS, was synthesized *via* the solution displacement method coupled with freeze-drying for the proof of concept described above (Fig. S2, ESI†). In a typical synthesis, nanocellulose suspensions were first prepared by chemically pretreating and mechanically treating wood to extract cellulose, followed by constructing a composite gel through depositing $SrTiO_3$:Al dispersion onto the suspension surface. Subsequently, the suspension was exchanged with LiCl solution and freeze-dried to produce NLS-x. Physical pictures of NL and NLS-20 clearly demonstrate that both samples contracted and formed concave mirror-shaped aerogels after freeze-drying (Fig. S3, ESI†). In stark contrast to NL, NLS-20 exhibits gray spots on its upper surface, attributed to $SrTiO_3$:Al (Fig. S3b, ESI†). The fluffy, multilayered structure, is primarily composed of hydrophilic NFC, significantly enhancing the interfacial area with air (Fig. 2a). The NFC also creates sub-millimeter pores crucial for rapid water vapor transport and storage (Fig. S4 and Table S1, ESI†). In contrast, the upper surface of NLS gel is covered by cubic $SrTiO_3$:Al particles with few pores (Fig. 2b).[17] Notably, the

comparable Brunauer–Emmett–Teller specific surface areas of NL and NLS-20 suggests that $SrTiO_3$:Al primarily distributes in the upper layer rather than into the pores of NFC (Table S1, ESI†). Meanwhile, micrometer-sized hygroscopic LiCl particles are widely distributed throughout both the periphery and interior of the gel, maximizing surface area exposed to air for enhanced moisture absorption. The porous NFC network serves as a reservoir to store water, ensuring continuous, rapid, and extensive hygroscopic absorption (Fig. 2a, b, and Fig. S5, ESI†). Importantly, the $SrTiO_3$:Al layer effectively splits water molecules captured from the air by NLS, generating H_2 under sunlight irradiation. Transmission electron microscopy (TEM) images further confirm the partial interfacial contact between the gel and $SrTiO_3$:Al (Fig. 2c). Homogeneous distribution of Cl throughout the gel is evidenced by Fig. 2f, while the presence of Sr and Ti from $SrTiO_3$:Al verifies its distribution on the surface of NLS-20 gel (Fig. 2g and h).

X-ray diffraction (XRD) was employed to evaluate the crystallinity of NLS-x. As shown in Fig. 2j, NLS-20 exhibits a broad peak around 22.6°, corresponding to the (200) diffraction peak in natural cellulose I crystals. Additionally, peaks at 30.0° and 34.8° are ascribed to the (111) and (200) characteristic peaks of LiCl.[11,18] The peaks located at 32.4°, 46.5°, and 57.8° are attributed to the (110), (200), and (211) characteristic diffraction peaks of $SrTiO_3$:Al, respectively.[19] The XRD patterns of NLS-x clearly show characteristic peaks of both NL and $SrTiO_3$:Al, indicating their coexistence in NLS-x (Fig. S6, ESI†). The Fourier transform infrared (FTIR) spectroscopy was used to confirm the chemical composition of NLS-x (Fig. 2k and Fig. S7, ESI†). In the spectra of NL, the reflectance bands at 3460 cm^{-1} and 3300 cm^{-1} are assigned to stretching vibrations of liquid water and hydroxyl groups in cellulose. The band at 1659 cm^{-1} is ascribed to variable-angle vibration of crystallized water, characteristic of cellulose water absorption.[20] The vibrational peaks due to antisymmetric stretching of –CH_2 and symmetric stretching of –CH appeared at 2918 cm^{-1}, with in-plane bending vibrations of –CH_2 and –OCH occurring at 1429 cm^{-1}.[21] Furthermore, the peaks at 1305 cm^{-1}, 1018 cm^{-1}, and 897 cm^{-1} are assigned to the bending vibration of –CH, the stretching vibration of C–O–C sugar ring, and iso-head carbon (C1) vibration, respectively.[20,21] These characteristic peaks confirm the effective extraction of cellulose from wood. The spectra of NLS-x contain all the characteristic peaks of NL, as well as the Ti–O stretching vibration from $SrTiO_3$:Al,[22] further validating their coexistence and the structural integrity of cellulose in NLS-x (Fig. S7, ESI†). The X-ray photoelectron spectroscopy (XPS) analysis of NLS-x provides detailed insights into the chemical structures and bonding nature, consistent with XRD and FTIR spectroscopy results. Fig. S8a (ESI†) shows the survey spectra of NLS-x, demonstrating the existence of C, O, Li, Cl, Sr, and Ti. High-resolution elemental scans indicate that these elements are all in their typical chemical states in NLS-x (Fig. S8b–g, ESI†).[23–27] The binding energies of Sr 3d and Ti 2p exhibit slight shifts, whereas the binding energies of Li 1s and Cl 2p remain constant (Fig. S8b, c, f, and g, ESI†). This observation indicates that it is NFC, rather than LiCl, interacts with $SrTiO_3$:Al in NLS-x.
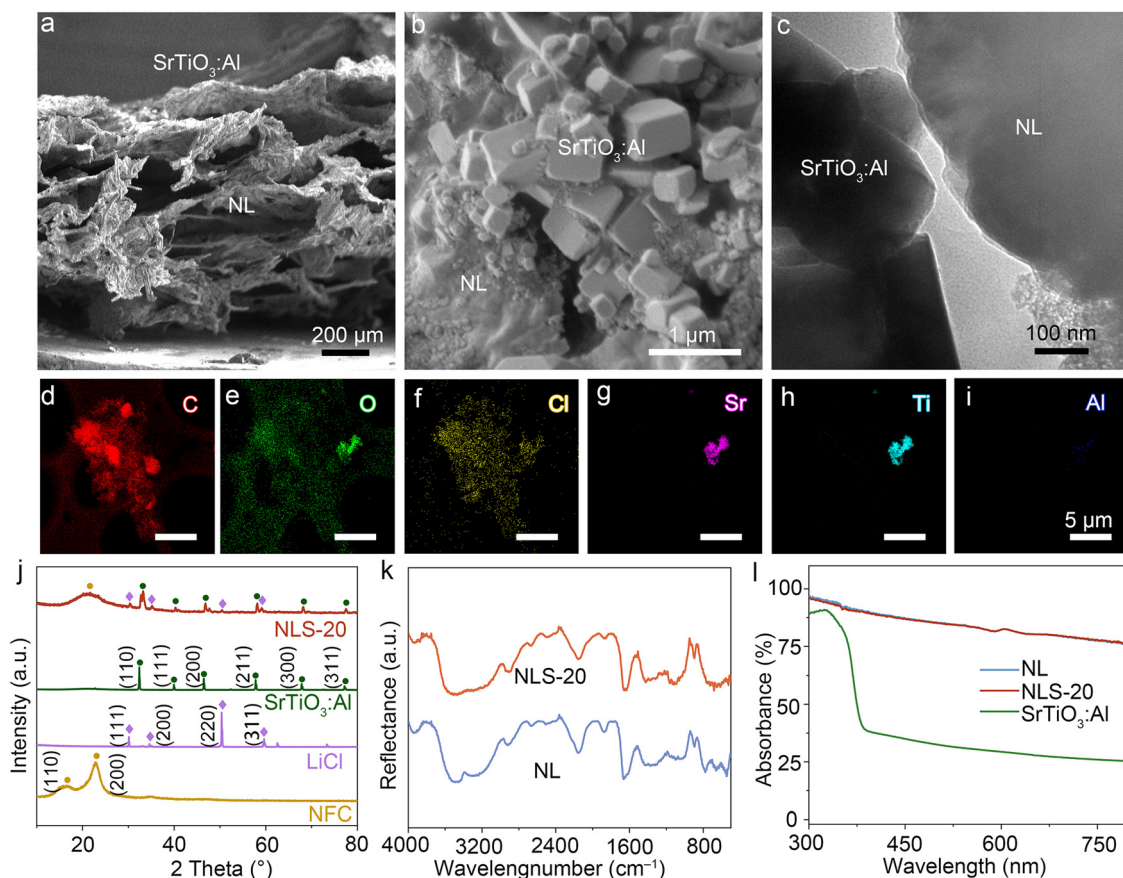
Fig. 2 Characterization of NL, NLS-20, and SrTiO$_3$:Al. Scanning electron microscopy (SEM) images of (a) cross-sectional view and (b) top surface, (c) TEM image, (d)–(i) corresponding energy-dispersive X-ray spectroscopy (EDX) mapping of C, O, Cl, Sr, Ti, and Al of NLS-20. (j) XRD patterns of the NFC, LiCl, SrTiO$_3$:Al, and NLS-20. (k) FTIR spectra of the NL and NLS-20, and (l) UV-vis spectra of the NL, NLS-20, and SrTiO$_3$:Al. Scale bar: (a) 200 μm, (b) 1 μm, (c) 100 nm, and (d)–(i) 5 μm.

All the NLS-*x* composites demonstrate remarkable light absorption (>75%), due to the loose porous structure of NFC (Fig. S9, ESI†). Specifically, NLS-20 exemplifies this outstanding light absorption property (Fig. 2l), which is crucial for solar-driven desorption of atmospheric water in conjunction with photocatalytic H$_2$ production. The process utilizes long-wave solar radiation for AWH and is complemented with short-wave radiation for photocatalytic H$_2$ production. This capability underscores their role in harnessing solar energy effectively for these sustainable processes. Furthermore, the steady-state photoluminescence analysis of NLS-*x* confirms efficient separation of photogenerated carriers (Fig. S10, ESI†), essential for their photocatalytic activity. Notably, the fluorescence signal of SrTiO$_3$:Al is obscured by that of NL, precluding the analysis of carrier migration kinetics of SrTiO$_3$:Al at NLS-20 using fluorescence data. In addition, the NLS-*x* composites present excellent physical and chemical stability, as evidenced by thermogravimetric analysis (TGA, Fig. S11, ESI†).

2.3. Solar-powered *in situ* H$_2$ production from air under varying humidity levels

In a proof-of-concept experiment, NLS-*x*, saturated with atmospheric moisture, were placed in a top-illuminated photoreactor depicted in Fig. S12 (ESI†), to utilize harvested water for *in situ* H$_2$

production driven by sunlight. The synergistic performance of NLS-*x* in both AWH and photocatalytic water splitting is of particular significance. The moisture uptake behavior of NLS-*x* was first investigated under controlled conditions by exposing the samples to a constant temperature and humidity chamber (40% RH, 25 °C). It was observed that the moisture absorption capacity of NLS-*x* at 40% RH could be up to 1.6–2.2 g_{H_2O} $g_{sorbent}^{-1}$, reaching equilibrium within approximately 10 h (Fig. 3a).

The outstanding hygroscopic behavior of NLS-*x* is attributed to the synergistic effect between hygroscopic salts and hydrophilic polymers. Specifically, a great number of LiCl particles dispersed throughout both the outer surface and interior of NLS-*x*. These LiCl particles capture atmospheric water molecules *via* chemisorption on the outer surface, where the hygroscopic nature of LiCl reduces vapor pressure at gel–air interface. In addition, water molecules penetrate into the interior through the open pores of NLS-*x*. This behavior is facilitated by plenty of hydrophilic functional groups within the NFC polymer network such as hydroxyl groups with lone-pair electrons and vacancies that act as donors and acceptors of hydrogen bonds, respectively, as well as interconnected pores which provide diffusion paths for surrounding water molecules. Furthermore, LiCl dispersed in the polymer pores continues to absorb water vapor from the air until NLS-*x*
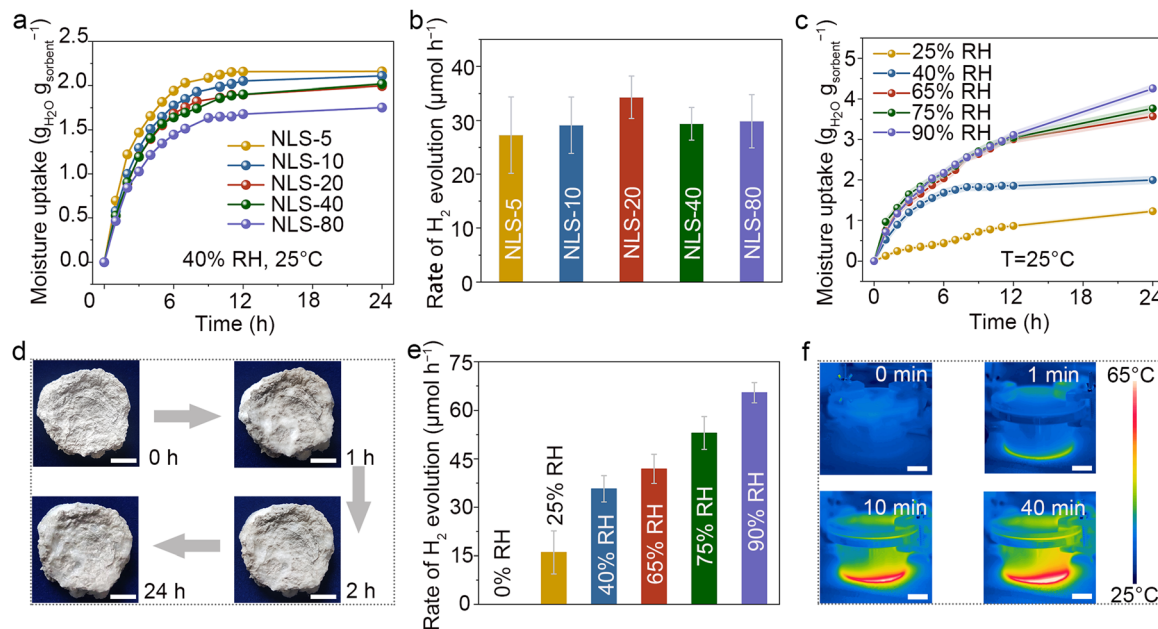
Fig. 3 Performance of solar-powered *in situ* H_2 production from full humidity air. (a) Moisture uptake of NLS-*x* samples for 24 h (25 °C, 40% RH). (b) The atmospheric water-splitting for H_2 production performance of NLS-*x* under Xe-lamp irradiation. Measurements were taken at least three times for separate samples and average values are presented with the standard deviation as the error bar. (c) Sorption kinetics of the NLS-20 at different RHs. (d) Digital photographs illustrate the process of atmospheric water absorption by NLS-20 at 90% RH. (e) H_2 production performance of NLS-20 under Xe-lamp irradiation *via* atmospheric water splitting after moisture sorption in different RHs. (f) Time-course infrared (IR) images of NLS-20 during H_2 production. Scale bar: (d) 1 cm and (f) 2 cm.

reaches saturation with hygroscopic water. The absorbed water rapidly diffuses into the NFC network, causing volume expansion. Although the incorporation of SrTiO$_3$:Al slightly reduces the affinity of the upper surface of NLS-*x* for water vapor (Fig. S13, ESI†), resulting in a modest attenuation of its hygroscopicity, overall, it maintains a leading position in water sorption capacity among reported state-of-the-art sorbents (Table S2, ESI†).

The atmospheric water captured synergistically by NFC and LiCl is continuously released under solar irradiation, facilitating photocatalytic water splitting over the surface of SrTiO$_3$:Al and producing H$_2$. The NLS-*x* composites exhibit outstanding photocatalytic activity for atmospheric water splitting activity when fully saturated with moisture absorption under ambient conditions (40% RH, 25 °C). As illustrated in Fig. 3b, these composites demonstrate remarkable ability for H$_2$ production, with the activity reaching a peak when the introduction of SrTiO$_3$:Al is optimized. Specifically, the H$_2$ production rate of NLS-*x* increases gradually with an appropriate amount of SrTiO$_3$:Al added ($x \leq 20$). Notably, NLS-20, when exposed to an air environment (40% RH, 25 °C), exhibits a maximum H$_2$ production rate of 34.3 μmol h^{-1} under simulated solar irradiation. Excess addition of SrTiO$_3$:Al ($x > 20$) leads to a reduction in H$_2$ production activity, probably due to a slight decrease in hygroscopicity. It is crucial to highlight that an optimal balance of hygroscopicity and photocatalytic activity is imperative for efficient conversion. Therefore, NLS-20 holds significant potential for H$_2$ production from air.

NLS-20 was then meticulously employed for AWH-H$_2$ production under different RH conditions. As illustrated in Fig. 3c–e, and Fig. S14 (ESI†), the hygroscopic capacity of NLS-20 increased

with rising RH levels, consequently enhancing its H$_2$ production activity. NLS-20 rapidly absorbsed water vapor, gradually wetting its surface (Fig. 3d). NLS-20 captured 1.23 g$_{H_2O}$ g$_{sorbent}$$^{-1}$ atmospheric water at 30% RH, resulting a H$_2$ production rate of 16.03 μmol h^{-1} and a corresponding STH of 0.07%. Notably, when saturated at 90% RH, NLS-20 presented a hygroscopic capacity of 4.26 g$_{H_2O}$ g$_{sorbent}$$^{-1}$, resulting in a photocatalytic activity of 65.45 μmol h^{-1}, among the highest reported for solar-driven *in situ* H$_2$ production from air (Tables S3 and S4, ESI†). The corresponding STH efficiency of NLS-20 is up to 0.3%. Fig. S15 (ESI†) illustrates the relationship between H$_2$ production and time, showcasing the continuous evolution of H$_2$ during the catalytic process. As shown in Table S5 (ESI†), the H$_2$ production rate of SrTiO$_3$:Al in the NLS-20 system is slightly lower than that in the suspension system, which can be attributed to the limited supply of atmospheric water. However, it is important to note that the NLS-20 is specifically designed for H$_2$ production in isolated, off-grid regions where purified liquid water is scarce, let alone H$_2$. The NLS system achieves *in situ* H$_2$ production using only natural moisture and sunlight. The NLS-20 is highly scalable for *in situ* H$_2$ production in full humidity environments. In principle, the outstanding photocatalytic performance of NLS-20 stems in part from its ability to facilitate the interfacial transfer of water vapor on the surface of the photocatalyst driven by solar energy (Fig. S16, ESI†). This design effectively reduces interfacial potential barriers and H$_2$ transport resistances in the biphasic reaction system.[28] Furthermore, the control experiment with unhygroscopic NLS-20 showed no detectable H$_2$ (Fig. 3e), confirming the origination of H$_2$ from the atmospheric water

molecules. Moreover, the temperature was maintained at around 60 °C during H_2 production, facilitating the generation of water vapour to construct the biphasic interface (Fig. 3f and Fig. S17, ESI†). Clearly, the engineered NLS-20 stands out for its unique advantage in efficiency H_2 production from air under varying humidity levels. The exceptional photocatalytic activity results from the effective combination of NFC and LiCl's hygroscopic characteristics with SrTiO$_3$:Al's robust light absorption and efficient carrier mobility.

To further validate the feasibility of *in situ* H_2 production from air, outdoor experiments utilizing NLS-20 were conducted. The NLS-20 performed excellent moisture uptake performance at 29%–45% RH (ambient temperatures of 28.6–31.6 °C), achieving 1.66 g_{H_2O} $g_{sorbent}^{-1}$ in the first 8 h and 2.10 g_{H_2O} $g_{sorbent}^{-1}$ in 24 h (Fig. 4a). The H_2 production device, which consists of NLS-20, H_2 detection tape, and a quartz glass enclosure, is lightweight and portable, making it suitable for off-grid regions (Fig. 4b). Notably, the color of the H_2 detection tape gradually changed from yellow to black, indicating continuous H_2 evolution under solar irradiation (Fig. 4c and Fig. S18, ESI†). During the period from 11:20 to 14:20, NLS-20 produced a total of 223.42 µmol of H_2 (Fig. 4d). The outdoor H_2 production performance is closely related to weather conditions, such as solar flux and ambient temperature (Fig. 4e).

As discussed above, the H_2 produced by NLS-20 originates from absorbed atmospheric water. However, no O_2 was detected during the entire H_2 production process from air, despite SrTiO$_3$:Al being recognized as a photocatalyst for overall water splitting. This raises the fundamental question of the whereabouts of the expected O_2. In Fig. 5a, we propose a plausible

reaction mechanism to address the query. In the NLS-20 system, SrTiO$_3$:Al absorbs photons exceeding its bandgap energy, thereby exciting electron–hole pairs that migrate to the surface reaction sites. Photogenerated electrons reduce protons at H_2-producing active sites to yield H_2, while photogenerated holes oxidize absorbed water vapor at O_2-producing active sites to produce reactive oxygen, resulting in ROS production. The energy band structure of SrTiO$_3$:Al satisfies the thermodynamic criteria for generating H_2O_2 and superoxide radicals ($^{\bullet}O_2^{-}$) by two-electron processes (Fig. S19, ESI† and Fig. 5b). Further verification of oxidation products utilized iodometric and *in situ* electron paramagnetic resonance (EPR) techniques, employing 5,5-dimethyl-1-pyrroline *N*-oxide (DMPO) as a trapping agent. The presence of H_2O_2 was confirmed in a 20-fold diluted aqueous solution, prepared from residual water post-H_2 production (Fig. S20, ESI† and Fig. 5c). Moreover, the H_2O_2 content in NLS-20 system after the H_2 production reaction was significantly higher compared to that before the reaction, demonstrating an expected continuous evolution of H_2O_2 in a catalytic process (Table S6 and Fig. S20c, ESI† Fig. 5c). Additionally, Fig. 5d illustrates observations from the NLS-20/methanol/DMPO system under simulated solar irradiation, revealing distinct signals indicating the presence of $^{\bullet}O_2^{-}$ radicals.[29] It is believed that the photogenerated holes of SrTiO$_3$:Al contributed significantly to the continuous formation of ROS, including H_2O_2 and $^{\bullet}O_2^{-}$, in NLS-20. The observed lack of O_2 production by SrTiO$_3$:Al in NLS-20 may stem from the limited interaction of SrTiO$_3$:Al with gaseous water in NLS-20, which further promotes gas separation.

The stability of NLS-20 significantly impacts its practical application of H_2 production from air. To assess its stability,
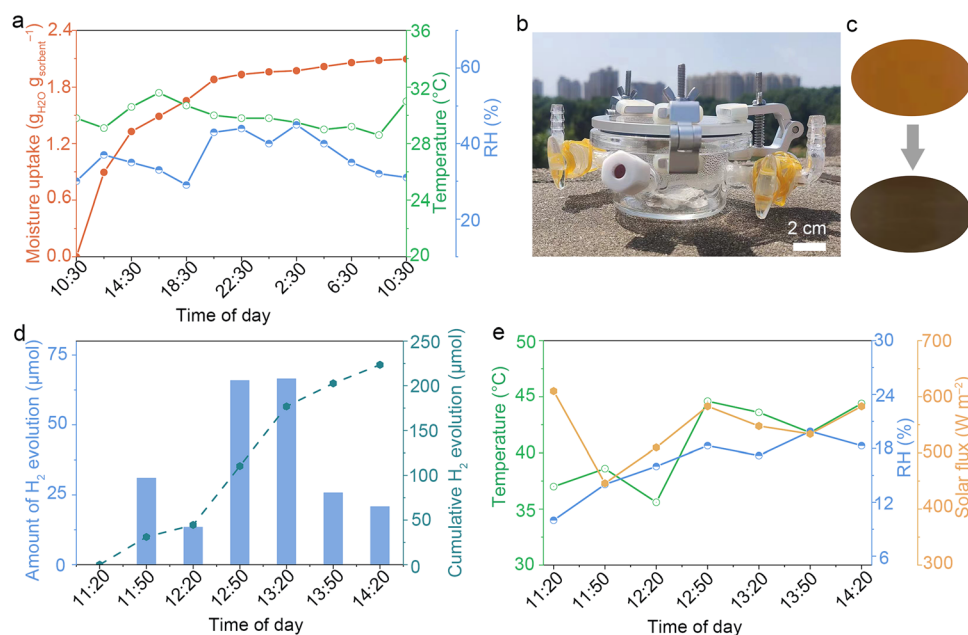

Fig. 4 Practical outdoor *in situ* H_2 production from air. (a) Diagram illustrating the moisture uptake performance of NLS-20, the corresponding ambient temperature, and RH. (b) Image of the H_2 production device utilizing NLS-20. (c) Enlarged view of the H_2 detection tape before (top) and after (bottom) the outdoor H_2 production reaction. (d) The atmospheric water-splitting for H_2 production using NLS-20 under outdoor sunlight irradiation. (e) Diagram showing the corresponding ambient temperature, RH, and solar flux. Scale bar: (b) 2 cm.
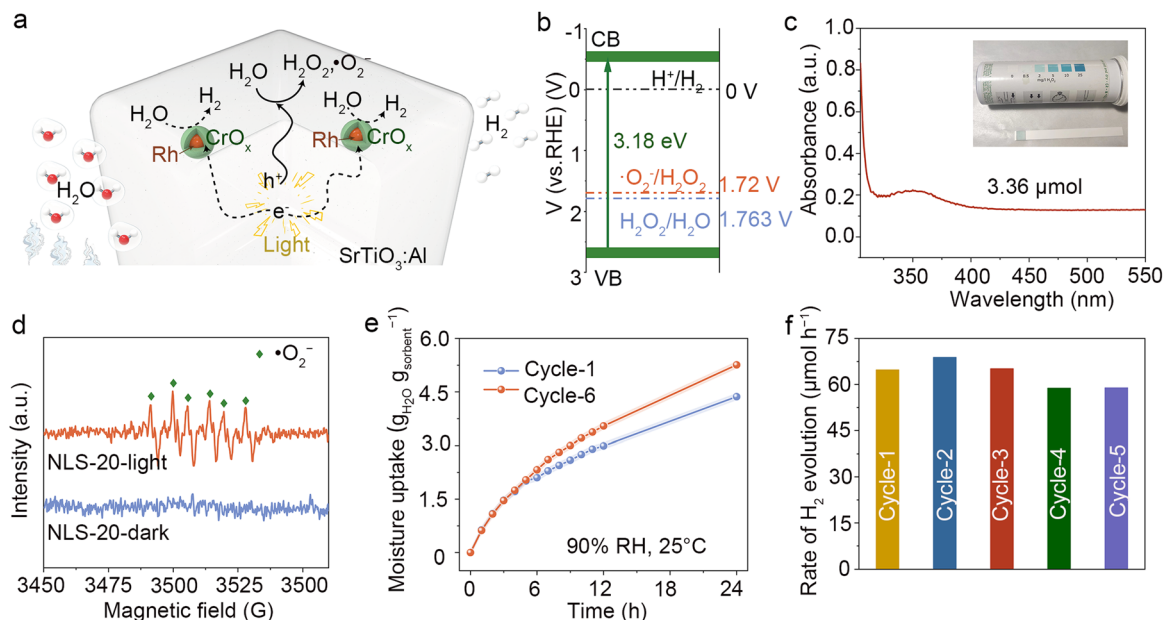
Fig. 5 Proposed photocatalytic mechanism and stability of NLS-20. (a) A schematic illustration of the proposed mechanism involved in the photocatalytic process for water vapour splitting over the $SrTiO_3$:Al catalyst in the NLS-20 system. (b) Electronic energy band structure of $SrTiO_3$:Al. (c) UV-vis spectrum of a 20-fold dilution of NLS-20 aqueous solution after H_2 production. (d) DMPO spin-trapping EPR spectra of NLS-20 under light irradiation in a methanol system. Stability test for (e) moisture uptake and (f) H_2 production by photocatalytic atmospheric water splitting on the NLS-20. Inset of (c) shows the digital photograph of H_2O_2 test paper, which reacted with an aqueous solution of NLS-20 after H_2 production.

hygroscopic saturated NLS-20 underwent several photocatalytic tests. As displayed in Fig. 5e, after 5 cycles of photocatalytic H_2 production, NLS-20 exhibited increased moisture uptake compared to its initial state, highlighting its remarkable moisture absorption stability. In principle, prolonged exposure of single LiCl to high humidity may lead to its dissolution, resulting in the loss of hygroscopic properties. However, in the NLS-20 system, the porous network structure of NFC disperses LiCl to prevent agglomeration, thereby providing excellent hygroscopic and regenerative properties for long-term applications in H_2 production from air (Fig. S1, ESI†). Importantly, the photocatalytic activity for atmospheric water splitting showed no discernible decrease over these cycles (Fig. 5f and Fig. S21, ESI†), underscoring the benefits derived from the excellent hygroscopicity and structural integrity of NLS-20. Moreover, minimal disparities were observed in XRD patterns, FTIR diffuse reflectance spectra, and XPS spectra of NLS-20 before and after water absorption-dehydration-H_2 production, indicating the chemical stability of its structure (Fig. S22–S24, ESI†). The FTIR diffuse reflectance spectra and high-resolution XPS profiles of Li 1s and Cl 2p for NLS-20 remain consistent before and after the reaction, ruling out the possibility of H_2O_2 being produced through the oxidation of cellulose and chlorides, respectively (Fig. S23, S24b, and c, ESI†). Morphologically, the similarity between pre- and post-reaction states was confirmed, with both showing rounded cubic $SrTiO_3$:Al embedded in the surface of gel polymer matrix, while LiCl particles distributed throughout its bulk (Fig. S25, ESI†). Furthermore, UV-vis spectra revealed negligible changes in the optical properties of NLS-20 before and after the reaction, affirming its stability under photocatalytic conditions (Fig. S26, ESI†).

Encouragingly, the concept of utilizing *in situ* resources, such as atmospheric water and solar energy, to produce H_2 has been successfully demonstrated. This innovation offers a new paradigm for efficient energy conversion and utilization in off-grid areas. However, several approaches could enhance the practical implementation of this system. The first approach involves modifying hygroscopic materials to improve moisture uptake performance and stability across a wide range of RHs. The second approach focuses on developing photocatalysts with improved catalytic activity, thereby enhancing H_2 production and reducing operational cycle time. The third method aims to create a microenvironment conducive to two-phase H_2 production by integrating modified hygroscopic materials with the catalyst. The last means emphasizes designing a device that synchronizes AWH with photocatalytic H_2 production, complemented by an additional unit for collecting gaseous fuel.

3. Conclusions

In summary, we have developed a bilayer NLS composite gel tailored for H_2 production from air with different humidity levels, employing a combination of solution displacement and freeze-drying methods. The gel's polymer framework incorporates cost-effective NFC extracted from wood, characterized by high density of hydroxyl groups that promote a layered porous architecture. This composition effectively mitigates LiCl aggregation during hydration, resulting in a remarkable hygroscopicity of 4.26 g_{H_2O} $g_{sorbent}^{-1}$ in 90% RH environment. The upper surface of the NLS gel features a layer of $SrTiO_3$:Al, which serves as a photocatalyst

capable of efficiently splitting atmospheric water, thereby facilitating H_2 production at a rate of 65.45 μmol h^{-1}, with a STH efficiency of up to 0.3%. This NLS design integrates mechanisms for self-supplying atmospheric water, optimizing light delivery and complementary utilization, ensuring facile H_2 evolution and stable catalyst immobilization. Overall, the NLS composite gel represents a significant advancement for mobile, distributed, community-managed, off-grid H_2 from air. It is anticipated that the innovative design will provide valuable insights into leveraging natural, *in situ* resources for sustainable green H_2 production.

Author contributions

The project was conceived and supervised by M. L., J. S., W. C., X. G., and X. Y., who designed the experiments and conducted initial characterization. Synthesis of SrTiO$_3$:Al photocatalysts was performed by L. T. and X. G., while TEM characterization was carried out by X. Y., L. T., and R. Z. X. Y. and F. X. designed *in situ* electron paramagnetic resonance experiments. Schematic illustrations were provided by J. H. and X. Y. Manuscript writing and revision were handled by X. Y., X. G., and M. L. All authors contributed to result discussion and manuscript development.

Data availability

The data supporting this article have been included as part of the ESI.†

Conflicts of interest

The authors declare no conflicts of interest.

Acknowledgements

References

1 R. Zheng, Z. Liu, Y. Wang, Z. Xie and M. He, *Joule*, 2022, **6**, 1148–1159.
2 T. He, P. Pachfule, H. Wu, Q. Xu and P. Chen, *Nat. Rev. Mater.*, 2016, **1**, 16059.
3 T. G. Deutsch, *Nat. Energy*, 2023, **8**, 560–561.
4 J. Lord, A. Thomas, N. Treat, M. Forkin, R. Bain, P. Dulac, C. H. Behroozi, T. Mamutov, J. Fongheiser, N. Kobilansky, S. Washburn, C. Truesdell, C. Lee and P. H. Schmaelzle, *Nature*, 2021, **598**, 611–617.
5 H. Kim, S. Yang, S. R. Rao, S. Narayanan, E. A. Kapustin, H. Furukawa, A. S. Umans, O. M. Yaghi and E. N. Wang, *Science*, 2017, **356**, 430–434.
6 Y. Zhang and S. C. Tan, *Nat. Sustainable*, 2022, **5**, 554–556.
7 S. Guo and S. C. Tan, *Joule*, 2024, **8**, 291–294.
8 Y. Liu, W.-K. Han, W. Chi, J.-X. Fu, Y. Mao, X. Yan, J.-X. Shao, Y. Jiang and Z.-G. Gu, *Appl. Catal., B*, 2023, **338**, 123074.
9 L. Huang, P. Liu, C. Qin, C. Gui, X. Zhang, T. Ren, Y. Ge, Y. Yu, Z. Liu and L. Chen, *Nano Energy*, 2024, **128**, 109879.
10 L. He, X. Zeng, H. Chen, L. Zhao, Z. Huang, D. Wang, X. He, W. Fang, X. Du and W. Li, *Adv. Funct. Mater.*, 2024, **34**, 2313058.
11 H. Shan, C. Li, Z. Chen, W. Ying, P. Poredoš, Z. Ye, Q. Pan, J. Wang and R. Wang, *Nat. Commun.*, 2022, **13**, 5406.
12 M. Wang, T. Sun, D. Wan, M. Dai, S. Ling, J. Wang, Y. Liu, Y. Fang, S. Xu, J. Yeo, H. Yu, S. Liu, Q. Wang, J. Li, Y. Yang, Z. Fan and W. Chen, *Nano Energy*, 2021, **80**, 105569.
13 M. Dai, F. Zhao, J. Fan, Q. Li, Y. Yang, Z. Fan, S. Ling, H. Yu, S. Liu, J. Li, W. Chen and G. Yu, *Adv. Mater.*, 2022, **34**, 2200865.
14 Q. Li, F. Wang, Y. Zhang, M. Shi, Y. Zhang, H. Yu, S. Liu, J. Li, S. C. Tan and W. Chen, *Adv. Mater.*, 2024, **36**, 2209479.
15 Y. Guo, W. Guan, C. Lei, H. Lu, W. Shi and G. Yu, *Nat. Commun.*, 2022, **13**, 2761.
16 W. H. Lee, C. W. Lee, G. D. Cha, B.-H. Lee, J. H. Jeong, H. Park, J. Heo, M. S. Bootharaju, S.-H. Sunwoo, J. H. Kim, K. H. Ahn, D.-H. Kim and T. Hyeon, *Nat. Nanotechnol.*, 2023, **18**, 754–762.
17 T. Takata, J. Jiang, Y. Sakata, M. Nakabayashi, N. Shibata, V. Nandal, K. Seki, T. Hisatomi and K. Domen, *Nature*, 2020, **581**, 411–414.
18 W. Chen, H. Yu, Q. Li, Y. Liu and J. Li, *Soft Matter*, 2011, **7**, 10360–10368.
19 Z. Zhao, E. J. Willard, H. Li, Z. Wu, R. H. R. Castro and F. E. Osterloh, *J. Mater. Chem. A*, 2018, **6**, 16170–16176.
20 E. Pretsch and M. B. P. Bühlmann, *Structure Determination of Organic Compounds*, Springer, Berlin Heidelberg, 2020.
21 M. C. Vieira, T. Heinze, R. Antonio-Cruz and A. M. Mendoza-Martinez, *Cellulose*, 2002, **9**, 203–212.
22 T. Xie, Y. Wang, C. Liu and L. Xu, *Materials*, 2018, **11**, 646.
23 J. Auvergniot, A. Cassel, D. Foix, V. Viallet, V. Seznec and R. Dedryvère, *Solid State Ion*, 2017, **300**, 78–85.
24 G. M. Dorris and D. G. Gray, *Cellul. Chem. Technol.*, 1978, **12**, 9–23.
25 Y. Liu, X. Xu, S. Zheng, S. Lv, H. Li, Z. Si, X. Wu, R. Ran, D. Weng and F. Kang, *Carbon*, 2021, **183**, 763–773.
26 Y. Liu, X. Xu, S. Lv, H. Li, Z. Si, X. Wu, R. Ran and D. Weng, *Catal. Sci. Technol.*, 2021, **11**, 3039–3046.
27 Z. Zhao, R. V. Goncalves, S. K. Barman, E. J. Willard, E. Byle, R. Perry, Z. Wu, M. N. Huda, A. J. Moulé and F. E. Osterloh, *Energy Environ. Sci.*, 2019, **12**, 1385–1395.
28 S. Guo, X. Li, J. Li and B. Wei, *Nat. Commun.*, 2021, **12**, 1343.
29 J.-L. Clément, N. Ferré, D. Siri, H. Karoui, A. Rockenbauer and P. Tordo, *J. Org. Chem.*, 2005, **70**, 1198–1203.